Original Research Paper   **Open Access Journal**

The Construction of Magnetic MnFe$_2$O$_4$@TpPa-1 Composite Materials and the Adsorption Removal Performance of Organic Pollutants in Solution

Shuai Wang*, Huifang Wang*, Luzeng Hu*, Zhipeng Lu*, Muqing Qiu* and Xin Zhong*†

*College of Life Science, Shaoxing University, Huancheng West Road 508, Shaoxing, 312000, P.R. China
†Corresponding author: Xin Zhong; zhongxinmagic@163.com

ABSTRACT

MnFe$_2$O$_4$@TpPa-1 adsorbent was developed by co-precipitation and solvothermal method, using β-ketoenamine linked covalent organic frameworks (COFs, TpPa-1) as supporting material to alleviate the aggregation of MnFe$_2$O$_4$. The properties were characterized by XRD, FT-IR, SEM, TEM, VSM, pH$_{pzc}$, and N$_2$ adsorption-desorption. The experimental results showed that the pseudo-second-order and Langmuir model best described the adsorption process, suggesting that the adsorption process was chemisorption and spontaneous endothermic reaction, and the maximum adsorption capacity of Bisphenol A (BPA) was 926.65 mg.g^{-1}. The main adsorption mechanism of BPA was hydrogen bonding and π-π conjugation between active functional groups in the TpPa-1 skeleton and BPA. Furthermore, the magnetic MnFe2O4@TpPa-1 showed good regeneration ability, indicating that MnFe2O4@TpPa-1 could be used in water treatment.

INTRODUCTION

In the past few decades, large numbers of toxic chemicals have been released into the environment due to the rapid industrialization and growth of the world population (Ji et al. 2015, Gómez-Pastora et al. 2017, Wacławek et al. 2017). These pollutants include azo dyes, antibiotics, endocrine disruptors, pesticides, and so on, most of which were persistent and not easily removed from natural ecosystems (Guan et al. 2013, Liu et al. 2014, Mohan et al. 2014, Liang et al. 2017, Guan et al. 2018). Furthermore, organic pollutants, particularly persistent ones with toxic, carcinogenic, and biorefractory functional groups, may pose a major threat to human health and ecological balance (Duan et al. 2015, Tian et al. 2018, Fu et al. 2019). Therefore, it is important to treat those pollutants effectively (Paethanom & Yoshikawa 2012; Tan et al. 2015, Abdel-Shafy & Mansour 2016, Li et al. 2018). At present, some treatment methods, such as adsorption, chemical reaction, bioremediation, etc. are applied to the organic pollutants in solution (Poletto 2016, Qiu et al. 2018, Rivas & Solís 2018, Jayawardhana et al. 2019, Wang et al. 2018, 2020).

Covalent organic frameworks (COFs) were first reported to be successfully produced in 2005 (Wang & Zhuang 2019). Since then, their properties have been investigated extensively. The main characteristics of COFs are (1) Low density, which is constructed by some light chemical elements such as C, H, O, N; (2) Regular pore structures that self-assemble into periodic and highly ordered pore formations. Thereby, their specific surface area, pore size, and pore shape could be easily adjusted; (3) Excellent chemical stability connected by covalent bond, resulting in considerably improved thermodynamic and chemical stability; (4) Diverse structure, synthesized by designing a variety of construction units and connection methods; (5) Functionalized, specific functional groups could be introduced to construction units in the initial stage (Wang & Zhuang 2019). Besides, COFs are the long-range orderly pore structure and crystalline organic porous materials, named as "Organic Zeolites". COFs materials application research in the environmental field is still in its early stages. COFs were mainly used for atmospheric governance research in the early research period. In recent years, it has been gradually applied to wastewater treatment (Liu et al. 2018).

COF-TpPa-1was selected, which was connected by imine bonds (-C=N-) and arranged periodically in a two-dimensional plane layer. Through - conjugation, interlayer covalent bond interlocking, and interlayer non-covalent interaction, COF-TpPa-1 was formed as a layer-by-layer structure in the plane and vertical direction (Kandambeth et al. 2012, He et al. 2017). TpPa-1 materials had excellent chemical stability. This advantage was particularly important for its application in the wastewater treatment industry.

However, the TpPa-1 material existed in powder form. The preparation procedure was complicated and the reaction conditions were harsh. As a result of these difficulties, its applicability in the field of water environment has been greatly limited. If $MnFe_2O_4$ was combined with TpPa-1, it could be compensated for each other in terms of application limitations. $MnFe_2O_4$ had a small specific surface area, while TpPa-1 had a high specific surface area, regular pores, and rich foreign elements. MnFe2O4 could also impart magnetic properties to powdered TpPa-1, allowing it to be easily recycled, reused, and at a lower cost. Furthermore, TpPa-1 could provide a carrier platform for $MnFe_2O_4$ particles to prevent their agglomeration. Therefore, combining TpPa-1 with $MnFe_2O_4$ not only enriched the types and properties of COFs but also made up for the application limitations of the TpPa-1 with $MnFe_2O_4$. This research could provide a new solution for wastewater treatment.

In this experiment, $MnFe_2O_4$@TpPa-1 adsorbent was developed by co-precipitation and solvothermal method, using β-ketoenamine linked covalent organic frameworks (COFs, TpPa-1) as supporting material to alleviate the aggregation of $MnFe_2O_4$. The properties were characterized by XRD, FT-IR, SEM, TEM, VSM, pHpzc, and N_2 adsorption-desorption. The adsorption experiments of Bisphenol A (BPA) by $MnFe_2O_4$@TpPa-1 were carried out. The adsorption mechanism and regeneration ability of BPA by $MnFe_2O_4$@TpPa-1 were discussed in detail.

MATERIALS AND METHODS

Materials

$MnCl_2 \cdot 4H_2O$, $FeCl_3 \cdot 6H_2O$, Arsenazo III, BPA, trialdehyde phloroglucinol (Tp), P-phenylenediamine (Pa), dioxane, acetic acid, methanol, and N,N-dimethyl formamide (DMF) were obtained from Shanghai Maclin Biochemical Technology Co., Ltd. HNO_3 and NaOH were purchased from Shanghai Chemical Reagent Co., Ltd. All the above reagents were of analytical grade or advanced purity and used directly without further purification. The ultrapure water was used in the experimental process.

Preparation of $MnFe_2O_4$

0.1 $mol \cdot L^{-1}$ Mn^{2+} ions and 0.2 $mol \cdot L^{-1}$ Fe^{3+} ions were prepared by $MnCl_2 \cdot 4H_2O$ and $FeCl_3 \cdot 6H_2O$, respectively. The mixture solution of 0.1 $moL \cdot L^{-1}$ Mn^{2+} ions and 0.2 $moL \cdot L^{-1}$ Fe^{3+} ions were added into the 250 mL of Erlenmeyer flask. Then, 100 mL 3 $mol \cdot L^{-1}$ NaOH solution slowly was added into the Erlenmeyer flask at a preheating temperature of 95°C. After continuous stirring and aging for 2 h, the solution was filtered, washed, and dried at 60°C for 12 h.

Preparation of $MnFe_2O_4$@TpPa-1

63 mg of Tp was dissolved into a mixture of (1+1) mesitylene and dioxane under ultrasonic conditions. Then, 100 mg of $MnFe_2O_4$ was added into the solution for 30 min under ultrasonic conditions. Then, 48 mg of Pa-1 was added into the solution for 30 min under ultrasonic conditions. Finally, 0.5 mL of 3 $mol \cdot L^{-1}$ acetic acid was added into the solution for 3 days at a temperature of 120°C. The supernatant was washed with DMF until it was clear. After that, they were washed twice more with acetone. Then, they were dried under vacuum at 80°C for 12 h. $MnFe_2O_4$@TpPa-1 was obtained for adsorption experiments.

Adsorption Experiments

Effect of pH: 2 mg of $MnFe_2O_4$ and 2 mg of $MnFe_2O_4$@TpPa-1 were added to 25 mL and 50 $mg \cdot L^{-1}$ of BPA solutions, respectively. The value of pH in the solution was adjusted from 1 to 10 with the 0.01 $mol \cdot L^{-1}$ HNO_3 or NaOH solution. Then, the mixture solution was put in a shaker at 25°C and 150 rpm for 24 h. The concentration of BPA was determined at equilibrium contact time.

Adsorption kinetics: 2 mg of $MnFe_2O_4$ and 2 mg $MnFe_2O_4$@TpPa-1 materials were added to 100 mL and 50 $mg.L^{-1}$ of BPA solution, respectively. The value of pH in the solution was adjusted to 2.0 with 0.01 $mol.L^{-1}$ HNO_3 solution. Then, the mixture solution was put in a shaker at 25°C and 150 rpm for 24 h. The concentration of BPA was determined at different contact time.

Adsorption thermodynamics: 2 mg of $MnFe_2O_4$ and 2 mg $MnFe_2O_4$@TpPa-1 materials were added to 100 mL and 15 $mg.L^{-1}$, 25 $mg.L^{-1}$, 50 $mg.L^{-1}$, 75 $mg.L^{-1}$, and 100 $mg.L^{-1}$ of BPA solution, respectively. The value of pH in the solution was adjusted to 2.0 with 0.01 $mol.L^{-1}$ HNO_3 solution. Then, the mixture solution was put in a shaker at a different temperature (25°C, 35°C, and 45°C) and 150 rpm for 24 h. The concentration of BPA was determined at equilibrium contact time.

Adsorption-desorption of the experiment: 2 mg of $MnFe_2O_4$ and 2 mg of $MnFe_2O_4$@TpPa-1 were added to 25 mL and 50 $mg.L^{-1}$ of BPA solutions, respectively. The value of pH in the solution was adjusted to 2.0 with 0.01 $mol.L^{-1}$ HNO_3 solution. Then, the mixture solution was put in a shaker at 25°C and 150 rpm for 24 h. The concentration of BPA was determined at equilibrium contact time. After the adsorption experiment was over, a magnet was used for solid-liquid separation. The obtained material was dried at 60°C for 12 h. Then, the obtained material was washed three times with methanol solution (Luo et al. 2019). After that, the above tests were repeated.

Analytical Method

The crystal structure of the sample was determined by X-Ray Diffraction (XRD) (Emoyrean diffractometer, Panalytical, Holland). The surface functional groups were detected by Fourier Transform Infrared Spectroscopy (FT-IR) (NEXUS). The morphology and particle size of the material were characterized by FE-SEM (Hitachi S4800) and TEM (FEI Tecnai F20 S-TWIN), respectively. The surface area and pore size distribution were measured by the N_2 adsorption-desorption method (ASAP 3020). Magnetic properties of materials were determined by Model 6000 (Quantum Design, USA). The surface charge properties of materials (Zeta potential) were determined by Malvern ZEN3690.

The concentration of BPA was measured by UV-spectrophotometer at 276 nm. The adsorption capacity of BPA by $MnFe_2O_4$/$MnFe_2O_4$@TpPa-1 was calculated using the following formula.

$$q_e = \frac{(C_0 - C_e)V}{m} \qquad \ldots(1)$$

Where, C_0 was initial concentration (mg.L^{-1}), C_e is the concentration at adsorption equilibrium (mg.L^{-1}), q_e is adsorption amount at adsorption equilibrium (mg.g^{-1}), V is the volume of solution (L), m is the mass of the adsorbent (g).

RESULTS AND DISCUSSION

The Characteristic of MnFe₂O₄@TpPa-1

The microstructure of the $MnFe_2O_4$@TpPa-1 was observed by SEM and TEM. The results are shown in Fig. 1. As shown from Fig.1(a), TpPa-1 was in the shape of a sea urchin. $MnFe_2O_4$ with a particle size of about 50 nm was distributed on the surface of TpPa-1. It could effectively prevent the accumulation of $MnFe_2O_4$. Additionally, the sea urchin-like morphology could give the $MnFe_2O_4$@TpPa-1 composite a high specific surface area and more adsorption sites. This structure facilitated its adsorption capacity.

Fig. 2(a) shows the FT-IR spectra of TpPa-1, $MnFe_2O_4$, and $MnFe_2O_4$@TpPa-1. The adsorption peaks at 3450 cm^{-1} and 1630 cm^{-1} were the O-H stretching vibration and bending vibration adsorption peaks, respectively.

This result indicated that the preparation of $MnFe_2O_4$ contained a large amount of –OH functional groups. The adsorption peaks at 430 cm^{-1} and 578 cm^{-1} corresponded to the characteristic peaks of Mn-O and Fe-O, respectively (Ghobadi et al. 2018). Compared with $MnFe_2O_4$, $MnFe_2O_4$@TpPa-1 not only had the above-mentioned characteristic adsorption peak but also had the characteristic peak of C=N
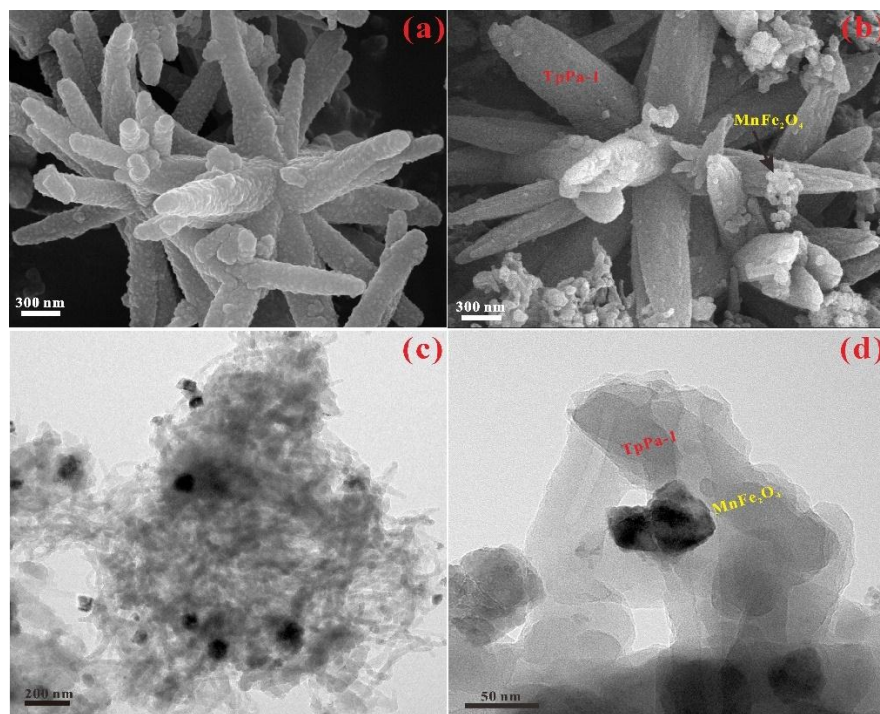

Fig. 1: SEM and TEM images of TpPa-1 and MnFe₂O₄@TpPa-1, SEM: (a) TpPa-1; (b) MnFe₂O₄TpPa-1; TEM: (c-d) MnFe₂O₄@TpPa-1
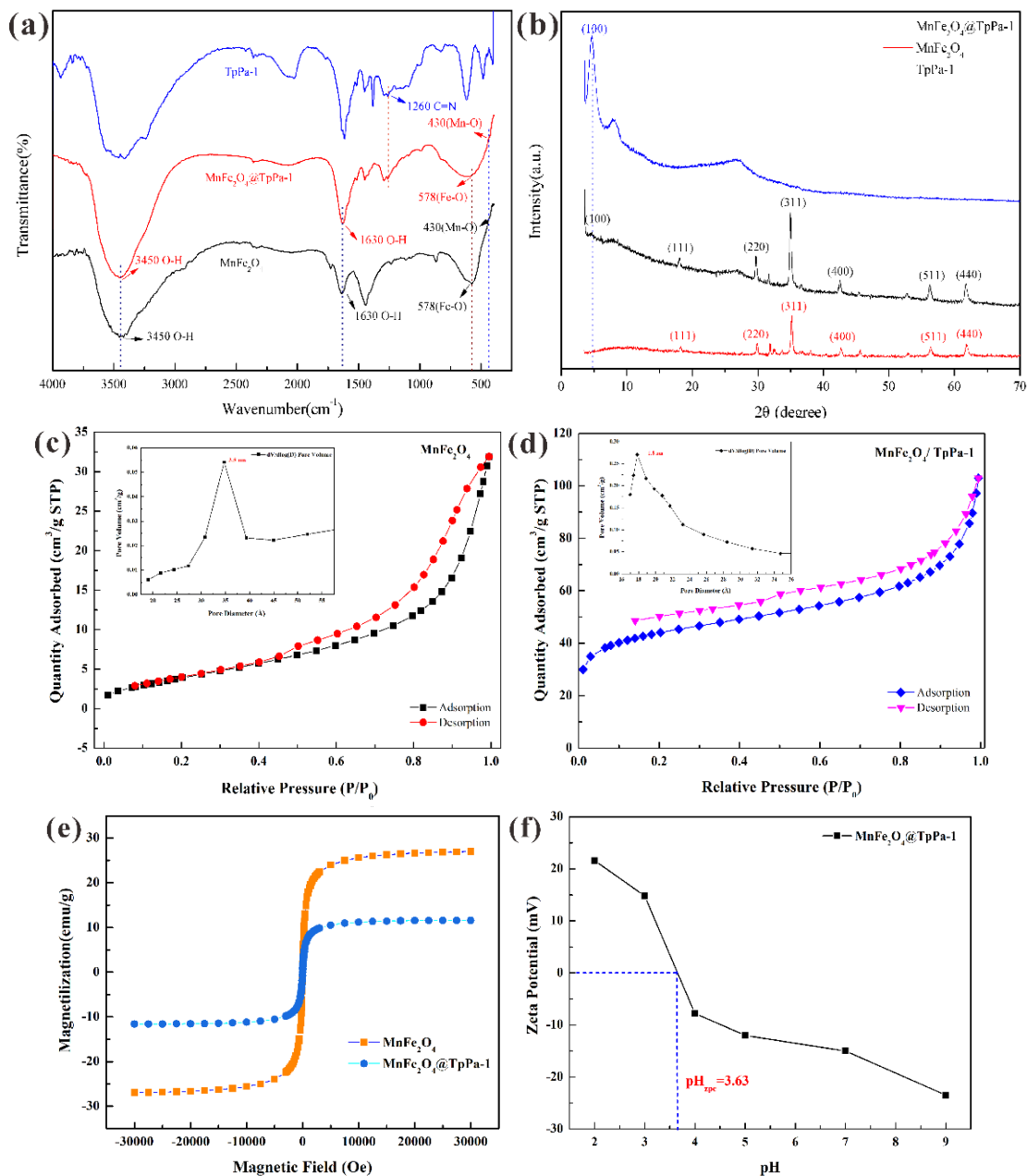
Fig. 2: (a) the FT-IR spectra of TpPa-1, $MnFe_2O_4$, and $MnFe_2O_4@TpPa-1$; (b) the XRD spectra of TpPa-1, $MnFe_2O_4$, and $MnFe_2O_4@TpPa-1$; N_2 adsorption-desorption isotherm of $MnFe_2O_4$ (c) and $MnFe_2O_4@TpPa-1$(d); (e) the magnetic hysteresis curves of $MnFe_2O_4$ and $MnFe_2O_4@TpPa-1$ at room temperature and (f) Zeta potential of $MnFe_2O_4@TpPa-1$.

at 1260 cm^{-1} which belongs to the framework of TpPa-1 (Kandambeth et al. 2012).

It indicated that $MnFe_2O_4@TpPa-1$ composite materials were successfully synthesized. The XRD spectra of TpPa-1, $MnFe_2O_4$, and $MnFe_2O_4@TpPa-1$ are shown in Fig.2(b). From the XRD pattern of $MnFe_2O_4$, some obvious diffraction peaks at 2θ =18.03º, 29.65º, 34.92º, 42.43º,

56.08º, and 61.56º could be observed. They corresponded to crystal planes (111), (220), (311), (400), (511), and (440), respectively, which were consistent with the standard card of $MnFe_2O_4$ (JCPDS Card NO. 10-0319) (Li et al. 2019). The XRD pattern of $MnFe_2O_4@TpPa-1$ was consistent with $MnFe_2O_4$. It indicated that $MnFe_2O_4$ maintained good crystallinity in the composite materials. Furthermore, the

diffraction peak of MnFe₂O₄@TpPa-1 at 2θ=4.7° was attributed to the (100) crystal plane of TpPa-1(Kandambeth et al. 2012). This result further proved that the MnFe₂O₄@TpPa-1 composite materials were successfully prepared.

Fig. 2(c-d) was the N_2 adsorption-desorption isotherm of MnFe₂O₄ and MnFe₂O₄@TpPa-1, respectively, and the internal inset figures were the pore size distribution diagram of MnFe₂O₄ and MnFe₂O₄@TpPa-1. The specific surface area, pore-volume, and pore size of MnFe₂O₄ were 15.4 $m^2.g^{-1}$, 0.04 $cm^3.g^{-1}$, and 3.5 nm, respectively. MnFe₂O₄@TpPa-1 composite materials had type IV isotherm. It suggested that it was a mesoporous material. Its specific surface area, pore, volume, and pore size were 235.5 $m^2.g^{-1}$, 0.17$cm^3.g^{-1}$, and 1.8 nm, respectively. The magnetic hysteresis curves of MnFe₂O₄ and MnFe₂O₄@TpPa-1 at room temperature are shown in Fig. 2(e). The saturation magnetization of the material was 26.94 and 11.52 $emu.g^{-1}$, respectively, which was sufficient to ensure the solid-liquid separation of the adsorbent and the aqueous solution under the condition of an external magnetic field (Hyun et al. 2012).

Effect of pH

To investigate the influence of pH on adsorption capacity, the adsorption experiments were carried out at a different pH in solution. Fig. 3 showed the effect of pH on the removal of BPA by MnFe₂O₄ and MnFe₂O₄@TpPa-1.

When pH was 2.0, the adsorption capacity of MnFe₂O₄ and MnFe₂O₄@TpPa-1 for BPA reached the maximum. When pH < 9.0, most BPA mainly existed in molecular form. However, when pH ≥ 9.0, BPA existed in the form of anionic BPA(HBPA⁻ and BPA²⁻). As shown from Fig. 2(f), the Zeta potential of MnFe₂O₄@TpPa-1 was 3.63. When the pH in the solution was lower than 3.63, the surface of MnFe₂O₄@TpPa-1 was positively charged. It indicated that
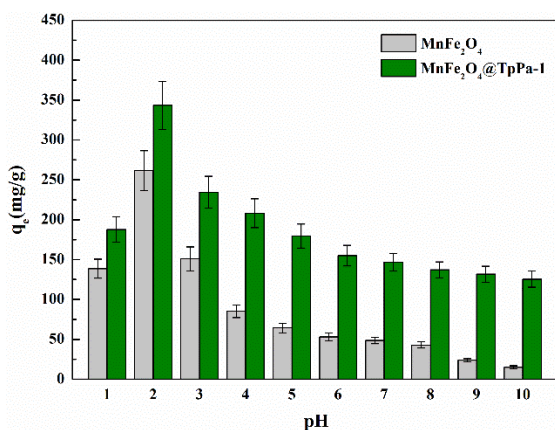
the removal of BPA mainly relied on π-π conjugation and hydrogen bonding (Zhong et al. 2020a, 2020b). When the pH of the solution was higher than 3.63, the surface of MnFe₂O₄@TpPa-1 was a negative charge. The electrostatic repulsion between MnFe₂O₄@TpPa-1 and BPA was enhanced, thereby reducing the amount of adsorption of BPA.

Adsorption Kinetics

The effect of contact time on the adsorption of BPA by MnFe₂O₄ and MnFe₂O₄@TpPa-1 are shown in Fig.4. It could be seen from Fig. 4(a) that the adsorption capacity of MnFe₂O₄ and MnFe₂O₄@TpPa-1 on BPA gradually increased with the increase of the reaction time. The adsorption capacity increased rapidly at the first stage of 30 minutes, and the adsorption sites on MnFe₂O₄ and MnFe₂O₄@TpPa-1 were continuously occupied. After 5 h, the adsorption sites on the surface tended to be saturated, causing the adsorption to gradually reach equilibrium. Compared with MnFe₂O₄, MnFe₂O₄@TpPa-1 had a higher adsorption capacity and faster adsorption rate for BPA. This was mainly the reason that MnFe₂O₄@TpPa-1 contained a higher specific surface area, larger pore volume, and various active surface functional groups (C=N, -OH, -NH₂) (Ding et al. 2015).

The pseudo-first-order, pseudo-second-order dynamic model, and intra-particle diffusion model were used to further explore the removal process of BPA by MnFe₂O₄ and MnFe₂O₄@TpPa-1. The pseudo-first-order model, the pseudo-second-order model, and the intra-particle diffusion model were as follows:

$$\ln(q_{e-}q_t) = \ln q_e - k_1 t \qquad \ldots(2)$$

$$\frac{t}{q_t} = \frac{1}{k_2 q_e^2} + \frac{t}{q_e} \qquad \ldots(3)$$

$$q_t = k_p t^{1/2} + C \qquad \ldots(4)$$

Where, q_e and q_t (mg.g⁻¹) are the adsorption capacity of BPA at equilibrium and t, respectively. k_1(min⁻¹), k_2(g min⁻¹mg⁻¹), and k_p (g/mg min^{0.5}) are the rate constants of the pseudo-first-order, pseudo-second-order dynamics model, and the intra-particle diffusion model, respectively. The results are shown in Fig. 4b-d and Table 1.

By comparing the correlation coefficient (R^2) value, it could be found that the pseudo-second-order kinetic model was more suitable for describing the adsorption process of BPA by MnFe₂O₄ and MnFe₂O₄@TpPa-1. It was suggested that the adsorption process was controlled by chemical adsorption or strong surface complexation. Furthermore, the internal particle diffusion model was used to study the adsorption and diffusion mechanism. The result is
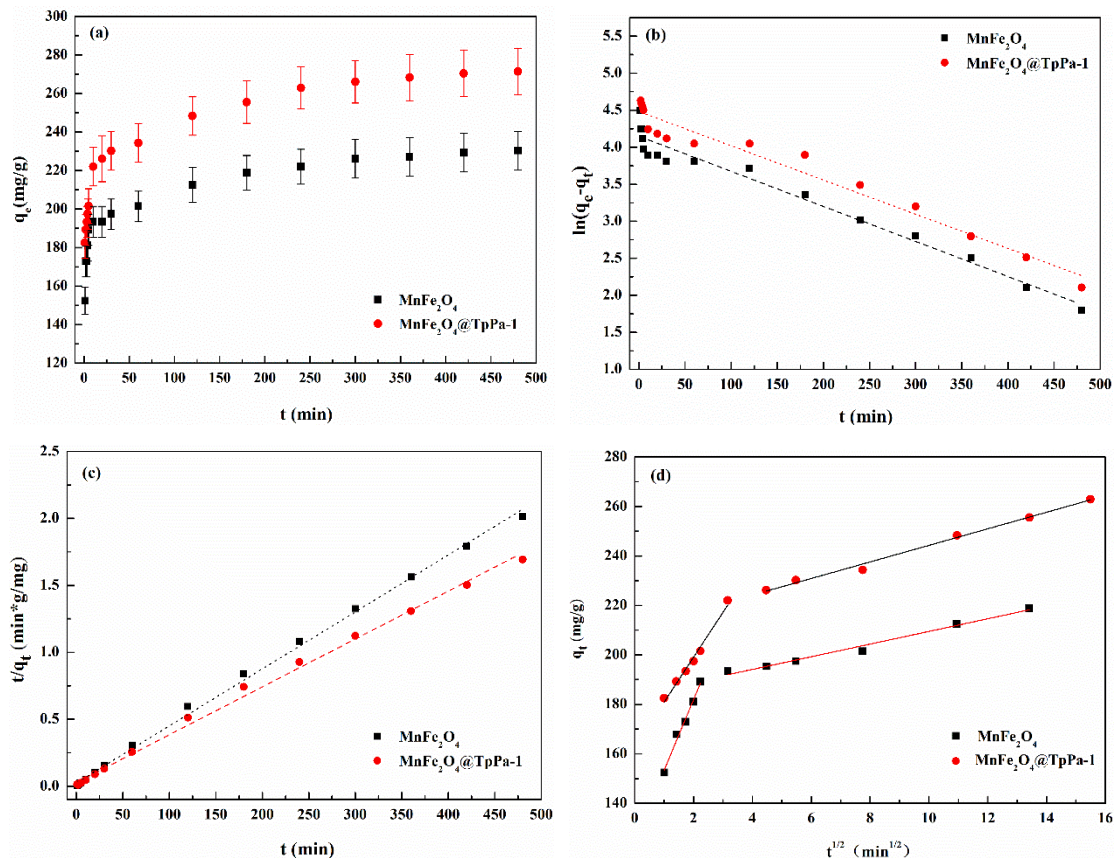

Fig. 3: Effect of pH on BPA adsorption onto MnFe₂O₄ and MnFe₂O₄@TpPa-1

Fig. 4: (a) Effect of contact time on the adsorption of BPA by $MnFe_2O_4$ and $MnFe_2O_4$@TpPa-1; (b) the pseudo-first-order model; (c) the pseudo-second-order model, and (d) the intra-particle diffusion model.

Table 1: The parameters of the kinetic models of BPA adsorption onto $MnFe_2O_4$ and $MnFe_2O_4$@TpPa-1.

Adsorbents	Pseudo-first-order			Pseudo-second-order			Intra-particle-diffusion		
	k_1 (min^{-1})	q_e (mg.g^{-1})	R^2	k_2 (g.mg$\cdot$min)	q_e (mg.g^{-1})	R^2	k_p (g.mg$\cdot$min$^{0.5}$)	C	R^2
$MnFe_2O_4$	0.005	63.43	0.9649	7.2×10^{-4}	238.09	0.9979	28.49	124.93	0.9809
							2.56	183.86	0.9810
$MnFe_2O_4$@TpPa-1	0.005	88.23	0.9604	4.7×10^{-4}	285.71	0.9967	18.14	162.80	0.9823
							3.35	210.80	0.9910

shown in Fig. 4(d). The fitting curve showed two-stage adsorption. Additionally, the fitting curve did not pass through the origin of the coordinate. It indicated that the adsorption process was affected by many factors. The first stage was the adsorption of BPA by $MnFe_2O_4$ and $MnFe_2O_4$@TpPa-1, which involved the instantaneous adsorption of BPA and film diffusion. In the second stage, internal diffusion occurs as BPA diffuses in the pores of $MnFe_2O_4$ and $MnFe_2O_4$@TpPa-1. Therefore, the adsorption process for BPA by $MnFe_2O_4$ and $MnFe_2O_4$@TpPa-1 was affected by chemical adsorption, strong surface complexation, and internal particle diffusion.

Adsorption Thermodynamics

The adsorption capacity of BPA by $MnFe_2O_4$ and $MnFe_2O_4$@TpPa-1 was investigated under the conditions of different initial concentrations of BPA and different temperatures (25°C, 35°C, and 45°C). The experimental results were fitted with Langmuir and Freundlich models, respectively (Equation 5 and Equation 6). The fitting results were shown

in Fig.5, and the relevant parameters were listed in Table 2.

$$Q_e = \frac{K_L Q_{max} C_e}{K_L C_e + 1} \quad \dots(5)$$

$$Q_e = K_F C_e^{1/n} \quad \dots(6)$$

Where, C_e (mg.L^{-1}) is the concentration at adsorption equilibrium. Q_e (mg.g^{-1}) is the amount of adsorption at adsorption equilibrium. Q_{max} (mg.g^{-1}) is the maximum adsorption capacity and K_L (L.mg^{-1}) is the constant of the Langmuir model. K_F and n are Freundlich constant.

The experimental results showed that the adsorption capacity of BPA by MnFe₂O₄ and MnFe₂O₄@TpPa-1 increased continuously with the increase of the initial concentration. By comparing the value of R², the Langmuir model was more fitted with the adsorption process of BPA by MnFe₂O₄ and MnFe₂O₄@TpPa-1. It indicated that the adsorption process of BPA was single-layer adsorption. Calculated by the Langmuir model, the maximum adsorption capacity of BPA by MnFe₂O₄ and MnFe₂O₄@TpPa-1 was 515.03 mg.g⁻¹ and 926.65 mg.g⁻¹, respectively.

Thermodynamic parameters of DG^0DH^0 and DS^0 were calculated by the formula (7-9). Fig. 6 shows the linear plots
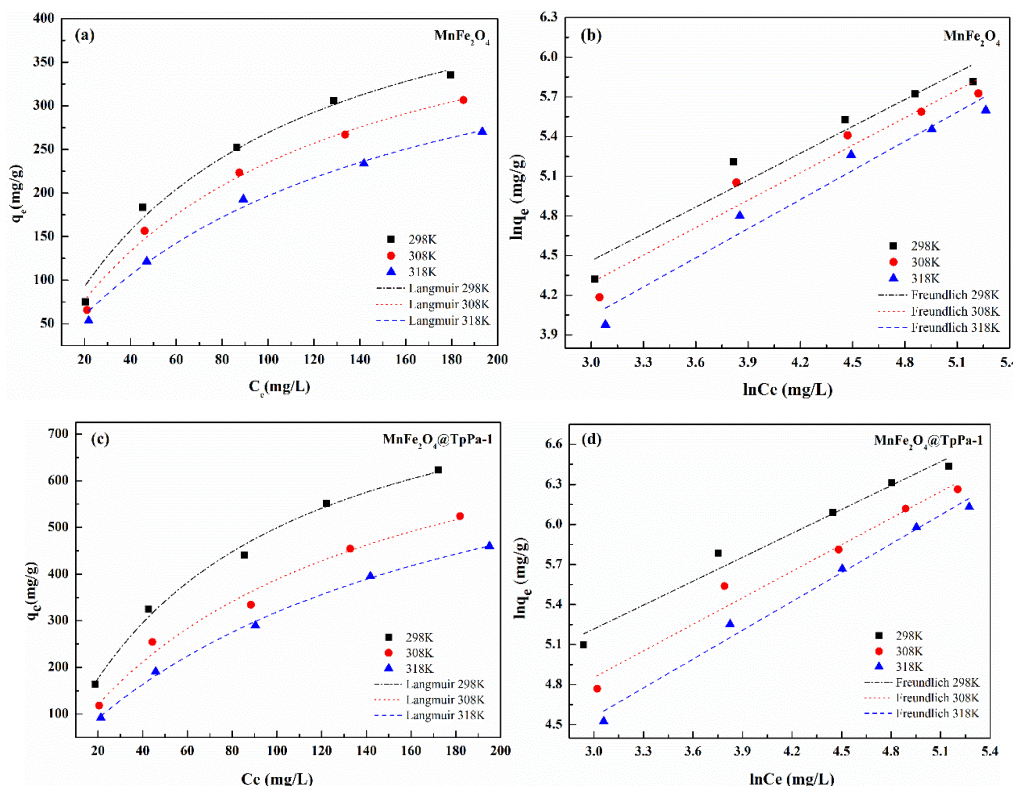

Fig. 5: The Langmuir model and Freundlich model of BPA adsorption onto MnFe₂O₄ (a-b) and MnFe₂O₄@TpPa-1(c-d).

Table 2: The parameters of Langmuir and Freundlich model for MnFe₂O₄ and MnFe₂O₄@TpPa-1 adsorption of BPA.

Adsorbents	T(K)	Langmuir model			Freundlich model		
		q_{max} (mg.g⁻¹)	K_L (L.mg⁻¹)	R^2	K_F (mg$^{1-1/n}$·g⁻¹·L$^{-1/n}$)	$1/n$	R^2
MnFe₂O₄	298	515.03	0.010	0.9823	11.32	0.677	0.9214
	308	482.47	0.009	0.9878	9.18	0.692	0.9351
	318	459.35	0.007	0.9906	6.29	0.734	0.9534
MnFe₂O₄@TpPa-1	298	926.65	0.011	0.9913	30.75	0.596	0.9705
	308	877.12	0.007	0.9805	17.53	0.662	0.9632
	318	866.28	0.005	0.9973	11.02	0.719	0.9835
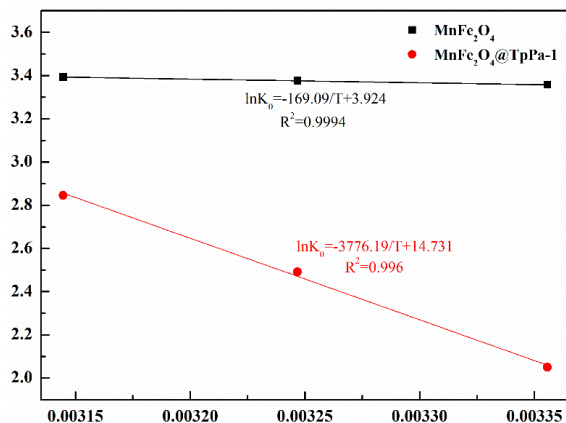
Fig. 6: The linear plots of $\ln K_0$ versus 1/T at three different temperatures (T = 298-318K).

Fig. 7: The adsorption-desorption cycles of $MnFe_2O_4$ and $MnFe_2O_4@$TpPa-1.

of $\ln K_0$ versus 1/T at three different temperatures. Thermodynamic parameters of BPA adsorption onto $MnFe_2O_4$ and $MnFe_2O_4@$TpPa-1 are listed in Table 3.

$$\Delta G^0 = -RT \ln K_0 \qquad \ldots(7)$$

$$\Delta G^0 = \Delta H^0 - T\Delta S^0 \qquad \ldots(8)$$

$$\ln K_0 = \frac{\Delta S^0}{R} - \frac{\Delta H^0}{RT} \qquad \ldots(9)$$

At different temperatures, the calculated ΔG^0 values were all less than zero and decreased as the temperature increased. It was suggested that the adsorption process is a spontaneous reaction. However, the values of ΔH^0 were all positive, indicating that the adsorption process was an endothermic reaction. The main reaction mechanism was the chemical adsorption process. In addition, the values of ΔS^0 were all greater than zero, indicating that the degree of the disorder increased at the solid-liquid interface.

Adsorption-Desorption of Experiment

The biggest disadvantage of COFs as adsorbents is the relatively high price of synthetic raw materials. In actual application, the cost of adsorbent is a very important
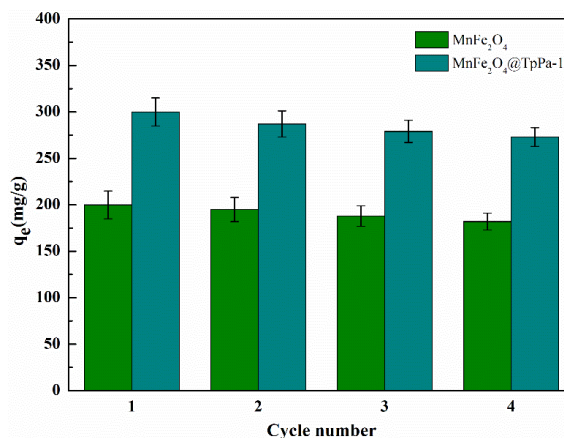
economic factor. Therefore, it is very important to investigate the recycling performance of composite materials, to reduce the cost of adsorbent used. The adsorption-desorption cycles of $MnFe_2O_4$ and $MnFe_2O_4@$TpPa-1 are shown in Fig. 7.

In this study, $MnFe_2O_4$ and $MnFe_2O_4@$TpPa-1 are used for four cycles. After four cycles of recycling, the adsorption of $MnFe_2O_4$ and $MnFe_2O_4@$TpPa-1 on BPA gradually decreased. It might be due to the depletion of active functional groups and non-renewable active sites during the adsorption process. However, $MnFe_2O_4@$TpPa-1 had a relatively high level of adsorption. It indicated that $MnFe_2O_4@$TpPa-1 had good regeneration ability. Therefore, it had good application prospects.

CONCLUSIONS

In this experiment, $MnFe_2O_4@$TpPa-1 composite material with high specific surface area, pore volume, and abundant active functional groups was prepared. $MnFe_2O_4@$TpPa-1 showed excellent adsorption capacity of BPA and good application prospects. In the research of adsorption kinetic, the pseudo-second-order kinetic model was more suitable to

Table 3: Thermodynamic parameters of BPA adsorption onto $MnFe_2O_4$ and $MnFe_2O_4@$TpPa-1.

Adsorbents	T(K)	$-\Delta G^0$ (kJ.mol^{-1})	ΔS^0 (J.(mol·K)$^{-1}$)	ΔH^0 (kJ.mol^{-1})
$MnFe_2O_4$	298	4.84	24.32	2.41
	308	5.08		
	318	5.32		
$MnFe_2O_4@$TpPa-1	298	5.10	122.47	31.40
	308	6.33		
	318	7.56		

describe the adsorption process of BPA by $MnFe_2O_4@TpPa$-1. It indicated that the adsorption process was controlled by chemical adsorption or strong surface complexation. In the research of adsorption thermodynamics, the Langmuir model was more fitted to the adsorption process of BPA by $MnFe_2O_4@TpPa$-1. It was suggested that the adsorption process was chemical adsorption, and the adsorption process was a spontaneous and endothermic reaction. The maximum adsorption capacity of Bisphenol A (BPA) was 926.65 mg.g^{-1}. The main adsorption mechanism of BPA was hydrogen bonding and π-π conjugation between active functional groups in the TpPa-1 skeleton and BPA. In addition, magnetism $MnFe_2O_4@TpPa$-1 exhibited good regeneration ability, indicating $MnFe_2O_4@TpPa$-1 had good regeneration ability, indicating that $MnFe2O4@TpPa$-1 could be used in water treatment.

ACKNOWLEDGEMENTS

REFERENCES

Abdel-Shafy, H.I. and Mansour, M.S.M. 2016. A review on polycyclic aromatic hydrocarbons: source, environmental impact, effect on human health and remediation. Egypt. J. Pet., 25: 107-123.

Ding, C.C., Cheng, W.C., Sun, Y.B. and Wang, X.K. 2015. Novel fungus-Fe_3O_4 bio-nano composites as high-performance adsorbents for the removal of radionuclides. J. Hazard. Mater., 295: 127-137.

Duan, X., Sun, H., Kang, J., Wang, Y., Indrawirawan, S. and Wang, S. 2015. Insights into heterogeneous catalysis of persulfate activation on dimensional-structured nanocarbons. ACS Catal., 5: 4629-4636.

Fu, H.C., Ma, S.L., Zhao, P., Xu, S.J. and Zhan, S.H. 2019. Activation of peroxymonosulfate by graphitized hierarchical porous biochar and $MnFe_2O_4$ magnetic nanoarchitecture for organic pollutants degradation: Structure dependence and mechanism. Chem. Eng. J., 360: 157-170.

Ghobadi, M., Gharabaghi, M., Abdollahi, H., Boroumand, Z. and Moradian, M. 2018. $MnFe_2O_4$-Graphene oxide magnetic nanoparticles as a high-performance adsorbent for rare earth elements: Synthesis, isotherms, kinetics, thermodynamics, and desorption. J. Hazard. Mater., 351: 308-316.

Gómez-Pastora, J., Dominguez, S., Bringas, E., Rivero, M.J, Ortiz, I. and Dionysiou, D.D. 2017. Review and perspectives on the use of magnetic nano photocatalysts (MNPCs) in water treatment. Chem. Eng. J., 310: 407-427.

Guan, R., Yuan, X., Wu, Z., Jiang, L., Li, Y. and Zeng, G. 2018. Principle and application of hydrogen peroxide-based advanced oxidation processes in activated sludge treatment: a review. Chem. Eng. J., 339: 519-530.

Guan, Y., Ma, J., Ren, Y., Liu, Y., Xiao, J., Lin, L. and Zhang, C. 2013. Efficient degradation of atrazine by magnetic porous copper ferrite catalyzed peroxymonosulfate oxidation via the formation of hydroxyl and sulfate radicals. Water Res., 47: 5431-5438.

He, S., Zeng, T., Wang, S., Niu, H. and Cai, Y. 2017. Facile synthesis of the magnetic covalent organic framework with a three-dimensional bouquet-like structure for enhanced extraction of organic targets. ACS Appl. Mater. Interf., 9: 2959-2965.

Hyun, S.P., Davis, J.A., Sun, K. and Hayes, K.F. 2012. Uranium(VI) reduction by iron(II) monosulfide mackinawite. Environ. Sci. Technol., 46: 3369-3376.

Jayawardhana, Y., Gunatilake, S.R., Mahatantila, K., Ginige, M.P. and Vithanage, M. 2019. Sorptive removal of toluene and m-xylene by municipal solid waste biochar: simultaneous municipal solid waste management and remediation of volatile organic compounds. J. Environ. Manag., 238: 323-330.

Ji, Y., Dong, C., Kong, D., Lu, J. and Zhou, Q. 2015. Heat-activated persulfate oxidation of atrazine: implications for remediation of groundwater contaminated by herbicides. Chem. Eng. J., 263: 45-54.

Kandambeth, S., Mallick, A., Lukose, B., Mane, M.V., Heine, T. and Banerjee, R. 2012. Construction of crystalline 2D covalent organic frameworks with remarkable chemical (acid/base) stability via a combined reversible and irreversible route. J. Am. Chem. Soc., 134: 19524-19527.

Li, C., Chen, C., Lu, J., Cui, S., Li, J., Liu, H., Li, W. and Zhang, F. 2018. Metal-organic framework derived $CoMn_2O_4$ catalyst for heterogeneous activation of peroxymonosulfate and sulfanilamide degradation. Chem. Eng. J., 337: 101-109.

Li, N., Li, W. and Fu, F. 2019. Removal of chromium (VI) by $MnFe_2O_4$ and ferrous ion: synergetic effects and reaction mechanism. Environ. Sci. Pollut. Res., 26: 30498-30507.

Liang, P., Zhang, C., Duan, X., Sun, H., Liu, S., Tade, M.O. and Wang, S. 2017. An insight into metal-organic framework derived N-doped graphene for the oxidative degradation of persistent contaminants: formation mechanism and generation of singlet oxygen from peroxymonosulfate. Environ. Sci.: Nano, 4: 315-324.

Liu, S., Xie, J., Su, Q., Du, G., Zhang, S., Cao, G., Zhu, T. and Zhao, X. 2014. Understanding Listorage mechanism and performance of $MnFe_2O_4$ by in situ TEM observation on its electrochemical process in nano lithium battery. Nano Energy, 8: 84-94.

Liu, Z., Wang, H., Ou, J., Chen, L. and Ye, M. 2018. Construction of hierarchically porous monoliths from covalent organic frameworks (COFs) and their application for bisphenol A removal. J. Hazard. Mater., 355: 145-153.

Luo, Z., Chen, H., Wu, S., Yang, C. and Cheng, J. 2019. Enhanced removal of bisphenol A from aqueous solution by aluminum-based MOF/sodium alginate-chitosan composite beads. Chemosphere, 237: 124493-124511.

Mohan, D., Sarswat, A., Ok, Y.S. and Pittman, C.U. 2014. Organic and inorganic contaminants removal from water with biochar, a renewable, low cost and sustainable adsorbent: A critical review. Bioresour. Technol., 160: 191-202.

Paethanom, A. and Yoshikawa, K. 2012. Influence of pyrolysis temperature on rice husk char characteristics and its tar adsorption capability. Energies, 5: 4941-4951.

Poletto, M. 2016. Thermogravimetric analysis and kinetic study of pinewood pyrolysis. Brazilian J. Wood Sci., 7: 111-118.

Qiu, M.Q., Wang, M., Zhao, Q.Z., Hu, B.W. and Zhu, Y.L. 2018. XANES and EXAFS investigation of uranium incorporation on nZVI in the presence of phosphate. Chemosphere, 201: 764-771.

Rivas, F.J. and Solís, R.R. 2018. Chloride promoted oxidation of tritosulfuron by peroxymonosulfate, Chem. Eng. J., 349: 728-736.

Tan, X., Liu, Y., Zeng, G., Wang, X., Hu, X., Gu, Y. and Yang, Z. 2015. Application of biochar for the removal of pollutants from aqueous solutions. Chemosphere, 125: 70-85.

Tian, W., Zhang, H., Sun, H., Tadé, M.O. and Wang, S. 2018. One-step synthesis of flour-derived functional nanocarbons with hierarchical pores for versatile environmental applications. Chem. Eng. J., 347: 432-439.

Wacławek, S., Lutze, H.V., Grübel, K., Padil, V.V.T., Černík, M. and Dionysiou, D.D. 2017. Chemistry of persulfates in water and wastewater treatment: A review. Chem. Eng. J., 330: 44-62.

Wang, H., Yang, N.C. and Qiu, M.Q. 2020. Adsorption of Cr(VI) from aqueous solution by biochar-clay derived from clay and peanut shell. J. Inorg. Mater., 35: 301-308.

Wang, J. and Zhuang, S. 2019. Covalent organic frameworks (COFs) for environmental applications. Coordin. Chem. Rev., 400: 213046.

Wang, W., Deng, S., Ren, L., Li, D., Wang, W., Vakili, M., Wang, B., Huang, J., Wang, Y. and Yu, G. 2018. Stable covalent organic frame2 works as efficient adsorbents for high and selective removal of an aryl-organophosphorus flame retardant from water. ACS Appl. Mater. Interf., 10: 30265-30272.

Zhong, X., Liang, W., Lu, Z. and Hu, B.W. 2020a. Highly efficient enrichment mechanism of U(VI) and Eu (III) by covalent organic frameworks with intramolecular hydrogen bonding from solutions. Appl. Surf. Sci., 504: 144403.

Zhong, X., Lu, Z., Liang, W. and Hu, B.W. 2020b. The magnetic covalent organic framework as a platform for high-performance extraction of Cr (VI) and bisphenol a from aqueous solution. J. Hazard. Mater., 393: 122353.